Spectral tuning of double resonant nanolaminate plasmonic nanoantennas with a fixed size

E. Mejia, Y. Qian, S. A. Safiabadi Tali, et al.

View Online   Export Citation   CrossMark

ARTICLES YOU MAY BE INTERESTED IN

AIP Publishing

Spectral tuning of double resonant nanolaminate plasmonic nanoantennas with a fixed size

View Online   Export Citation   CrossMark

E. Mejia,[1] Y. Qian,[1] S. A. Safiabadi Tali,[1] J. Song,[1,2] and W. Zhou[1,a)]

AFFILIATIONS

[1]Department of Electrical and Computer Engineering, Virginia Tech, Blacksburg, Virginia 24061, USA
[2]Physical Measurement Laboratory, National Institute of Standards and Technology, Gaithersburg, Maryland 20899, USA

[a)]Author to whom correspondence should be addressed: wzh@vt.edu

ABSTRACT

Multiresonant plasmonic nanoantennas can enhance nanolocalized multiphoton processes or enable wavelength-multiplexed nano-optic operations by supporting multiple spatially overlapped plasmonic modes. Nevertheless, current multiresonant plasmonic nanoantenna designs do not consider engineering multiresonant spectral responses with strict size and footprint constraints. Developing a strategy to engineer fixed-size nanoantennas with tunable multiresonant responses is highly desirable for maintaining controlled cellular responses at the nano-bio interface and achieving seamless integration with other nanodevices with predefined footprints. Here, we report that fixed-size tapered nanolaminate nanoantennas (TNLNAs) can achieve a wide double-resonance spectral tunability by only changing the metal-to-insulator thickness ratio (t/h). Three separate TNLNAs' samples (8/38, 20/20, and 28/8 nm) with a nominal total height of ∼100 nm are created from a high-throughput nanofabrication technique. Specifically, we fabricated TNLNAs' samples by exploiting a nanohole array membrane from soft interference lithography as a deposition mask for electron-beam evaporation of alternating Au and SiO_2 layers. Transmission and dark field scattering measurements show that TNLNAs support two distinct resonant features with t/h-dependent tunable resonant wavelengths in the range of 730–850 and 840–1050 nm, respectively. Numerical simulations reveal that (i) a bianisotropy-induced magnetoelectric response in top and bottom nanogaps due to the asymmetric tapered shape can enhance light trapping and achieve optical near-field intensity enhancements up to 1000-fold and (ii) while TNLNAs consisting of thin Au nanodisks at low t/h primarily support spatial overlap between modes with enhanced electric polarizability, TNLNAs consisting of thick Au nanodisks at high t/h support spatial overlap between modes with enhanced magnetic polarizability, evoking higher-order multipolar behaviors.

Plasmonic nanoantennas (PNAs) can support localized surface plasmon (LSP) modes to concentrate and transduce optical energy at deep subwavelength scales.[1–6] PNAs with optimized single-resonant near-field characteristics are sufficient for applications based on single-photon excitation/emission processes such as photothermal conversion, hot carrier generation, elastic/inelastic scattering, and photoluminescence.[7–9] However, for applications based on multiphoton processes or wavelength-multiplexed operations, it is highly desirable to engineer multiresonant PNAs to enhance nanolocalized optical processes in two or more wavelength bands.[10]

Currently, there are several strategies to engineer the multiresonant response of PNAs. First, PNAs of high aspect ratios and large sizes can support multiple high-order modes from phase retardation effects.[11,12] Second, planar composite PNAs consisting of optically coupled plasmonic nanoresonators can support multiple hybridized LSP modes.[13–16] Third, core-shell PNAs can support multiple hybridized LSP modes at multiple metal-dielectric interfaces.[17–20] Whether relying on near-field interactions or a collection of self-similar yet different sized plasmonic building blocks, engineering and structurally tuning the multiresonant response typically involve changing the physical size/shape or 2D spatial arrangement of the constituent PNAs. Consequently, the vast majority of reported multiresonant PNAs relying on in-plane or core-shell geometric engineering are unsuitable for hybrid integration with other types of optical or electronic nanodevices with predefined footprint geometries.[21] Along this direction, there are two key aspects to consider: fabrication and design degrees of freedom to achieve spectral tunability for multiresonant nanoantennas. For fabrication, a high-throughput CMOS-compatible fabrication technique is crucial to enable scalable fabrication for the widespread use of integrated hybrid platforms beyond the lab research purpose. For design degrees of freedoms, it remains to be determined whether a tunable multiresonant response can be attained when all

characteristic design parameters (size, shape, and spacing) are predefined. These two considerations are especially critical for hybrid biomedical applications targeting cells for the following two reasons. First, the scalable nanofabrication can enable direct integration of fixed-size tunable PNAs with other types of nanodevices, such as micro-/nanoelectrodes, to achieve multimodal operations at the nano-bio interface.[22,23] Second, minimizing nanodevice geometry variations at the nano-bio interface in an ordered array can promote controlled cellular responses to increase biomedical experiments' reproducibility.[24]

A suitable candidate to alleviate existing PNAs' design challenges can be sandwich-like nanolaminate metal-insulator-metal (MIM) nanostructures. By supporting a high-energy antibonding electric dipole (ED) mode and a low-energy bonding magnetic dipole (MD) mode, MIM nanostructures can serve as building blocks to construct metamaterials, metasurfaces, and composite nanoantennas.[25,26] Since the nanolithography-based fabrication process typically involves using nanoholes as a deposition mask for physical vapor evaporation of alternating metal and dielectric layers, MIM nanostructures develop tapered sidewalls due to gradually closing nanoholes as a material accumulates at the top edges. In turn, the inversion symmetry at the surface is broken, opening rich hybridization schemes between vertically stacked nonidentical resonators. However, despite initial investigations on the plasmonic hybridization process in nanolaminate PNAs,[27–36] there is still a lack of experimental work to investigate the geometric tunability of multiresonant responses under strict size/footprint constraints for asymmetrical nanolaminate nanoantennas.

In this Letter, we report that fixed-size tapered-shape nanolaminate nanoantennas (TNLNAs) can achieve a spectrally tunable double-resonant response by solely controlling the metal-to-insulator thickness ratio. We fabricated dense arrays of TNLNAs by electron-beam assisted evaporation of alternating Au and SiO_2 layers of varying thicknesses through nanohole array deposition masks. Extinction and dark-field scattering (DFS) spectroscopic measurements show that TNLNAs can support two widely tunable LSP modes with geometric dependence on the Au-to-SiO_2 thickness ratios. Furthermore, finite-difference time-domain (FDTD) simulations reveal that the geometry-dependent spectral tunability originates from modified resonant properties of elementary electric and magnetoelectric modes in their vertically stacked building blocks as well as their mutual coupling strength.

Figure 1(a) illustrates the soft-lithography nanofabrication process to create dense TNLNAs on glass substrates (see the supplementary material). Briefly, we employed the PEEL technique (photolithography, etching, e-beam evaporation, and lift-off)[37] to fabricate gold nanohole array (AuNHA) thin films with a nanohole diameter of ≈130 and a film thickness of ≈120 nm to serve as a deposition mask to obtain TNLNAs. One wafer-scale AuNHA mask was cut into ∼2 × 2 cm^2 pieces and used in the deposition of three different TNLNAs with t/h conditions of $t_{8 nm}/h_{38 nm}$, $t_{20 nm}/h_{20 nm}$, and $t_{28 nm}/h_{8 nm}$, with the fixed total height of ∼100 nm [Fig. 1(b)].

To examine the far-field response of fixed-size TNLNAs with different t/h ratios, we performed extinction measurements [Fig. 1(c)]
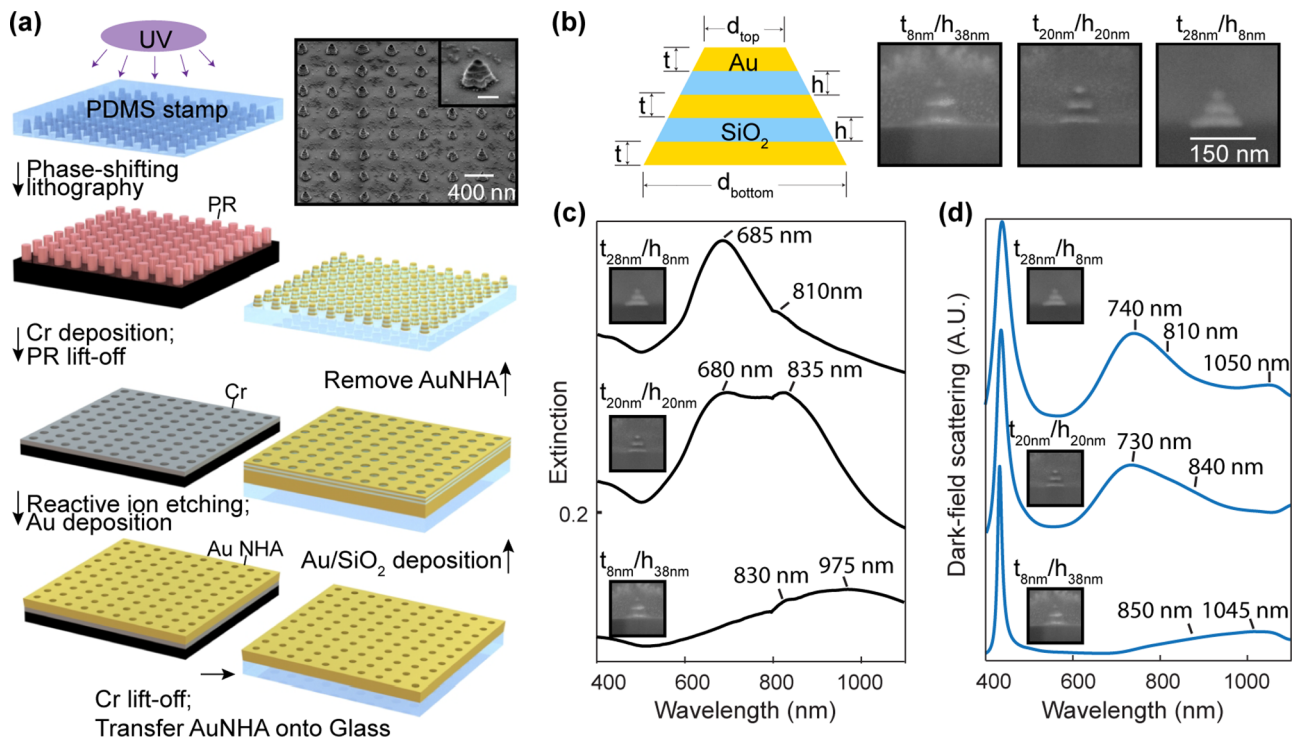
FIG. 1. Fixed-size tapered-shape nanolaminate plasmonic nanoantennas (TNLNAs). (a) Scheme of the fabrication process and tilted-view scanning electron microscope (SEM) images of TNLNAs. Inset scale bar: 60 nm. (b) Cross-sectional schematic and SEM images of fixed-size TNLNAs with different Au-to-SiO_2 thickness ratios (t/h). (c) Measured normal-incidence extinction spectra and (d) dark-field scattering spectra for fixed-size TNLNAs with three different Au-to-SiO_2 thickness ratios (t/h: 8/38, 20/20, and 28/8 nm).

using a UV-Vis-NIR spectrophotometer and dark-field scattering (DFS) measurements [Fig. 1(d)] using a dark-field micro-reflectance setup (Fig. S1). For the $t_{8\,nm}/h_{38\,nm}$ TNLNAs, extinction shows an extensively broad peak feature at ≈975 nm with an additional resonant feature at ≈830 nm. DFS reveals a peak at ≈1045 nm and a shoulder feature at ≈850 nm. For the $t_{20\,nm}/h_{20\,nm}$ TNLNAs, extinction shows two partially overlapped resonant features at ≈680 and ≈835 nm, and DFS reveals a broad asymmetrical scattering peak feature at ≈730 nm and a shoulder tucked at ≈840 nm. For the $t_{28\,nm}/h_{8\,nm}$ TNLNAs, extinctions reveal a broad asymmetrical resonant feature at ≈685 nm with a gradually decaying line shape toward the NIR region that envelops two features (≈810 and ≈1000 nm). DFS reveals a significant peak at ≈740 nm and a broad asymmetrical line shape that indicates a feature at ≈810 and ≈1050 nm. Therefore, Figs. 1(c) and 1(d) experimentally demonstrate that the fixed-size TNLNAs exhibit a double-resonant response with a strong geometric dependence on the t/h ratios between the spectral range of 400 and 1100 nm. Additionally, all three TNLNAs with different t/h show an absorption peak feature at a wavelength range less than 520 nm due to the Au interband electronic transition from the d band to the sp band.[38] Interestingly, all three TNLNAs exhibit a sharp emission peak at 440 nm in DFS measurements [Fig. 1(d)], which originates from electron–hole pair radiative recombination following light absorption by the interband electronic transition in Au.[38,39]

To connect far-field measurements with near-field optical properties, we performed FDTD simulations of the fixed-size TNLNAs

with different t/h ratios (Fig. 2). In the extreme case that h = 0, TNLNAs turn into a tapered Au nanoparticle (AuNP) of the same size. There is a reasonably good match between the FDTD-calculated and measured spectral profiles for the AuNP and three TNLNAs samples. The measured resonant features show broader linewidths than their FDTD-calculated counterparts due to deposition-related broadening effects.[26] The calculated scattering spectra of TNLNAs do not show the observed emission peak at 440 nm, because the FDTD package used for calculations is a linear system solver and thus does not capture the nonlinear photoluminescence from interband electronic transitions in Au.[40]

Comparing the FDTD-calculated extinction, absorption, and scattering spectra of TNLNAs with different t/h and the Au NPs of the same size reveals several distinct features. First, while the Au NP shows a single-resonant response with dominant scattering losses, the fixed-size TNLNAs show double-resonant responses with significantly increased absorption losses. This observation indicates the TNLNAs' modes have different microscopic natures from the Au NP mode ($\lambda'_{NP} = 645$ nm). Second, the double-resonant responses of fixed-size TNLNAs strongly depend on t/h, and the two modes' resonant wavelengths and spectral features evolve differently with t/h changes. Calculated extinction spectra [Fig. 2(a)] reveal that as t/h increases, the high-energy mode resonant wavelength first blueshifts from $\lambda'_{top}(t_{8\,nm}/h_{38\,nm}) = 745$ to $\lambda'_{top}(t_{20\,nm}/h_{20\,nm}) = 637$ nm and then redshifts from $\lambda'_{top}(t_{20\,nm}/h_{20\,nm})$ to $\lambda'_{top}(t_{28\,nm}/h_{8\,nm}) = 705$ nm. Simultaneously, the
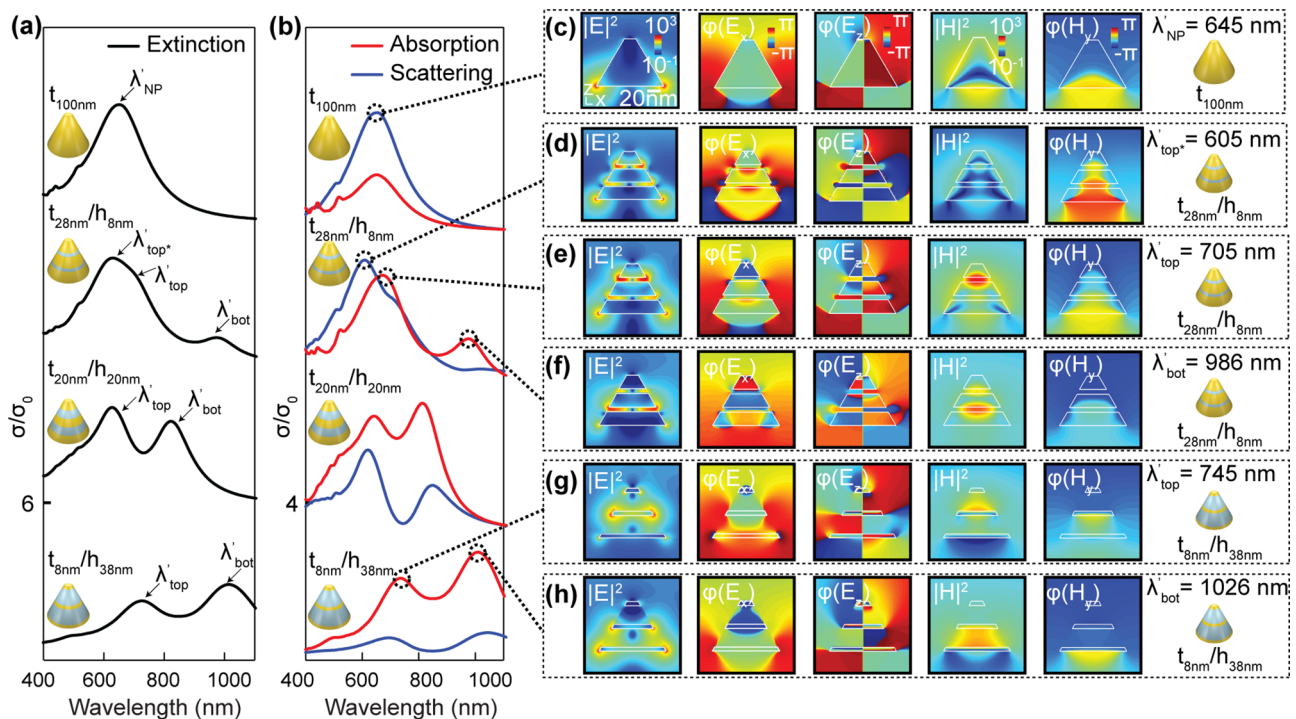
FIG. 2. Calculated far-field and near-field optical properties. (a) FDTD-calculated extinction cross section spectra and (b) absorption/scattering cross section spectra for fixed-size TNLNAs with four different Au-to-SiO₂ thickness ratios ($t_{100\,nm}$, $t_{8\,nm}/h_{38\,nm}$, $t_{20\,nm}/h_{20\,nm}$, and $t_{28\,nm}/h_{8\,nm}$). (c)–(h) FDTD-calculated distribution maps of $|E|^2$ and $|H|^2$ and phase distribution at resonant wavelengths of (c) 645, $t_{100\,nm}$, (d) 605, (e) 705, (f) 986, $t_{28\,nm}/h_{8\,nm}$, (g) 745, and (h) 1026 nm, $t_{8\,nm}/h_{38\,nm}$.

resonant wavelength of the low-energy mode first blueshifts from $\lambda'_{bot}(t_{8\,nm}/h_{38\,nm}) = 1026$ to $\lambda'_{bot}(t_{20\,nm}/h_{20\,nm}) = 806$ and then redshifts from $\lambda'_{bot}(t_{20\,nm}/h_{20\,nm})$ to $\lambda'_{bot}(t_{28\,nm}/h_{8\,nm}) = 986$ nm. Therefore, by engineering t/h ratios, the low-energy mode can be spectrally tuned in a broader wavelength range ($\Delta\lambda_{bot} \approx 200$ nm) than the high-energy mode ($\Delta\lambda_{top} \approx 100$ nm). Third, the relative contributions from scattering and absorption to the total mode losses are different between the high-energy and low-energy modes and depend on t/h ratios in fixed-size TNLNAs. Finally, for $t_{28\,nm}/h_{8\,nm}$ TNLNAs, the broad high-energy extinction feature at 680 nm is due to interference between a superradiant mode's scattering peak at 605 nm for $\lambda'_{top*}(t_{28\,nm}/h_{8\,nm})$ and a subradiant mode's absorption peak at 705 nm for $\lambda'_{top}(t_{28\,nm}/h_{8\,nm})$.[10]

To investigate the microscopic nature behind the far-field spectral features of Au NPs and fixed-size TNLNAs, we plotted near-field distribution maps of field intensities ($|E|^2$ and $|H|^2$) and phases [$\varphi(E_x)$, $\varphi(E_z)$, and $\varphi(H_y)$] for different modes as shown in Figs. 2(c)–2(h). For $t_{100\,nm}$ Au NPs [Fig. 2(c)], the resonant feature at λ'_{NP} manifests ED characteristics with a uniform $\varphi(E_x)$ within the Au NP, and it shows highly concentrated $|E|^2$ at the Au NP bottom edges, while the top Au interface almost remains unexcited.

We can find an increased spectral and spatial overlap between the simultaneously excited gap modes for $t_{28\,nm}/h_{8\,nm}$ to cause their interference, which is also reflected in the $\varphi(E_x)$ map [Fig. 2(d)] with $\approx\pi$

change centralized in the top and bottom gap. The optical response shows a dominant electric nature driven by the LSP at the metal-substrate interface. The high-energy scattering peak at $\lambda'_{top*}(t_{28\,nm}/h_{8\,nm})$ exhibits dominant ED characteristics [Fig. 2(d)]. Next, the high-energy absorption peak at $\lambda'_{top}(t_{28\,nm}/h_{8\,nm})$ exhibits multipolar characteristics because of the aforementioned inference effects but shows overall dominant MD characteristics in the top MIM nanogap [Fig. 2(e)]. Finally, the low-energy absorption peak at $\lambda'_{bot}(t_{28\,nm}/h_{8\,nm})$ shows electric and magnetic high-order multipolar characteristics with dominant MD characteristics in the bottom MIM nanogap [Fig. 2(f)].

For low t/h, the high-energy resonant feature at $\lambda'_{top}(t_{8\,nm}/h_{38\,nm})$ exhibits (i) EQ characteristics with roughly out-of-phase $\varphi(E_x)$ distribution between the top two Au nanodisks and (ii) MQ characteristics with out-of-phase $\varphi(H_y)$ between the two MIM nanogaps, yet the asymmetrical geometry gives rise to intense $|H|^2$ in the top MIM nanogap [Fig. 2(g)]. Comparatively, the low-energy resonant feature at $\lambda'_{bot}(t_{8\,nm}/h_{38\,nm})$ depicts (i) EQ characteristics with roughly out-of-phase $\varphi(E_x)$ distribution between the bottom and middle Au nanodisks and (ii) MD characteristics with a higher $|H|^2$ in the bottom MIM nanogap and with in-phase $\varphi(H_y)$ in the two MIM nanogaps [Fig. 2(h)], but the top MIM remains unexcited.

Unlike symmetric MIM building blocks supporting pure ED and MD modes, asymmetric TNLNAs can support magnetoelectric (ME) modes with bianisotropic responses due to the coupling between
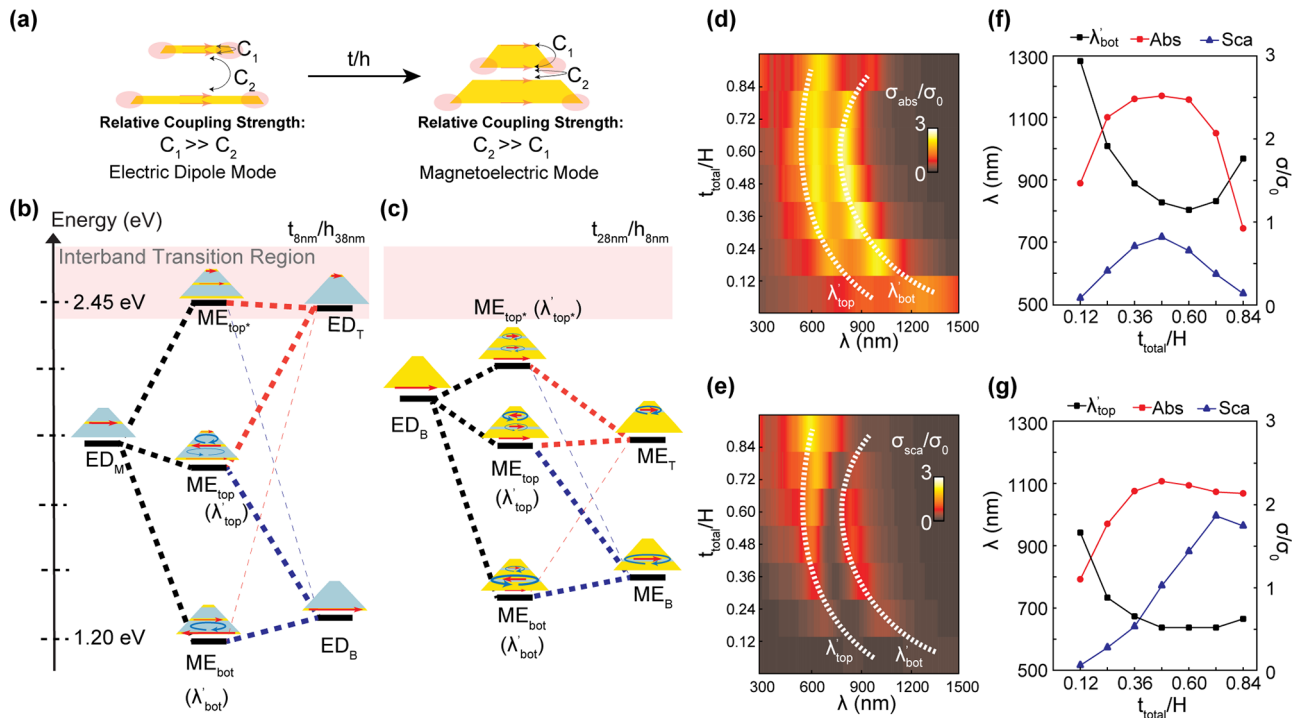

FIG. 3. Microscopic and macroscopic trends of hybridized modes in TNLNAs. (a) Illustration of elementary mode coupling for thin and thick metal layers in MIM building blocks. (b) and (c) Hybridization energy level diagram for (b) $t_{8\,nm}/h_{38\,nm}$ and (c) $t_{28\,nm}/h_{8\,nm}$. The red line-arrows and blue loop-arrows stand for the microscopic resonant sources with fundamental ED and MD characteristics. The arrow directions depict their relative phase relations, and the thickness stands for relative magnitude. (d) and (e) 2D color map as a function of total metal composition (t_{tot}/H) for normalized (d) absorption and (e) scattering cross sections. (f) and (g) The dependence of the resonant wavelength and the peak absorption/scattering cross sections on t_{tot}/H for (f) low-energy and (g) high-energy hybridized LSP modes.

nonorthogonal electric and magnetic polarizabilities.[41] ME modes become prominent as the nanogap decreases [Fig. 3(a)]. The dominant elementary mode is dependent on t/h, but based on the near-field characteristics, we can construct an energy level diagram for the extreme cases of $t_{8 nm}/h_{38 nm}$ [Fig. 3(b)] and $t_{28 nm}/h_{8 nm}$ [Fig. 3(c)]. For $t_{8 nm}/h_{38 nm}$ TNLNAs with a low t/h ratio, each metal disk supports an elementary low-energy bonding ED mode and a high-energy antibonding EQ mode (see the supplementary material).[27] Due to high LSP coupling strength within thin metals, the EQ mode for the bottom, middle, and top disks blueshifts to the higher energy region (300–520 nm) with significant damping from interband electronic transitions. Therefore, the optical response is mediated by the coupling among the top (ED_T), middle (ED_M), and bottom (ED_B) elementary ED modes, as illustrated in the energy diagram in Fig. 3(b). The middle ED_M mode can hybridize with the top ED_T mode to form a higher-energy ME mode [$ME_{top*}(\lambda'_{top*})$] with dominant ED characteristics and with the bottom ED_B mode to form a high-energy ME mode [$ME_{top}(\lambda'_{top})$] with dominant MD characteristics in the top gap. The coupling between the middle ED_M mode with both ED_T and ED_B modes leads to a hybridized ME mode [$ME_{bot}(\lambda'_{bot})$] with dominant MD characteristics in the bottom gap.

For $t_{28 nm}/h_{8 nm}$, the energy diagram in Fig. 3(c) considers that the mode sustained by the bottom metal-substrate interface (ED_B) can couple with the elementary mode from the top (ME_T) and bottom (ME_B) MIM blocks as separate subsystems (see the supplementary material). Because of its ME response with mutually coupled electric and magnetic polarizabilities, the ME_T mode in TNLNAs is nonorthogonal to the ED_B mode. Therefore, the ME_T and ED_B modes can further hybridize to generate a higher-energy mode [$ME_{top*}(\lambda'_{top*})$] with ED and MD characteristics and a high-energy mode [$ME_{top}(\lambda'_{top})$] with multipolar characteristics. Furthermore, ME_B can hybridize with ED_B to form a low-energy mode [$ME_{bot}(\lambda'_{bot})$] with dominant MD characteristics.

To understand how absorption and scattering losses evolve with increasing metal composition in TNLNAs, we have plotted the 2D maps [Figs. 3(d) and 3(e)] of absorption (σ_{abs}/σ_0) and scattering (σ_{sca}/σ_0) cross sections as a function of the ratio between the total metal thickness (t_{tot}) and the fixed total height ($H = 100$ nm), where $t_{tot} = 3t$ and $H = 3t + 2h$. The 2D map in Figs. 3(d) and 3(e) shows that the double-resonant response follows a parabolic-like shifting of λ'_{top} and λ'_{bot} from the NIR-Vis-NIR and shows that σ_{abs}/σ_0 and σ_{sca}/σ_0 appear to increase proportionally with t_{tot}/H for ME_{top}. For ME_{bot}, however, σ_{abs}/σ_0 and σ_{sca}/σ_0 appear to evolve similarly as ME_{top} but only up to a certain t_{tot}/H condition, which appears to correspond with the inflection point, where λ'_{bot} reverses course from a blueshifting to a redshifting trend. Both ME modes are dominated by the absorptive loss channel with significant Ohmic losses in the form of thermal dissipation. Maximizing the absorption cross section for nanoantennas is highly desirable for many biomedical applications based on photothermal processes, including plasmonic photothermal stimulation of electrogenic cells, plasmonic cell membrane optoporation for intracellular nanoprobe access or molecular cargo delivery, and photothermal tumor ablation for cancer therapy. On the other hand, for nanoantenna applications that prefer reduced absorption, possible solutions to minimize nonradiative losses for multiresonant TNLNAs include using post thermal annealing to reduce inelastic electron scattering at crystalline boundaries,[42] replacing gold with low loss

plasmonic materials like titanium nitride,[43] or assembling nanoantennas in ordered arrays to couple with delocalized lattice modes.[44]

Upon closer inspection, the scatter plots of the absorption and scattering cross sections [Figs. 3(f)–3(g)] reveal that as t_{tot}/H increases from 0.12 to 0.36 for ME_{bot}, λ'_{bot} blueshifts from 1283 to 890 nm, accompanied by an increase in σ_{sca}/σ_0 from 0.08 to 0.82 and an increase in σ_{abs}/σ_0 from 1.46 to 2.52. As t_{tot}/H increases from 0.36 to 0.6, λ'_{bot} gradually blueshifts to 805 nm, but then rapidly redshifts to 970 nm when t_{tot}/H increases beyond 0.60 to 0.84. Concurrently, the σ_{sca}/σ_0 for the ME_{bot} mode decreases to 0.14 and σ_{abs}/σ_0 decreases to 0.92 when t_{tot}/H increases from 0.48 to 0.84. As t_{tot}/H increases from 0.12 to 0.72 for the ME_{top} mode, λ'_{top} blueshifts from 946 to 617 nm and simultaneously, σ_{sca}/σ_0 increases from 0.06 to 1.86 and σ_{abs}/σ_0 increases from 1.09 to 2.28. As t_{tot}/H increases beyond 0.84, λ'_{top} redshifts to 669 nm and σ_{sca}/σ_0 decreases to 1.74 while σ_{abs}/σ_0 is maintained at 2.13. These observations suggest several critical points. First, the blueshift of λ'_{top} and λ'_{bot} as t_{tot}/H increases from 0.12 to 0.48 (low t/h) implies that the blueshifting of the elementary ED modes, which occurs as nanodisk t increases, dominates the overall spectral response. Second, there is a simultaneous competing redshift of the spectral response occurring as nanogap decreases, which begins to dominate as t_{tot}/H increases beyond 0.48 (high t/h), indicating a critical transition point where the increased splitting energy between ME_{bot} and ME_{top} modes results from the transition of a plasmonic system dominated by the ED mode of individual metallic nanodisks to the one dominated by the elementary ME mode of individual insulator nanogaps. Finally, the ME_{bot} mode has attributes of a dark (subradiant) mode of multipolar nature. It is typically challenging to be excited in in-plane plasmonic systems and requires breaking the in-plane geometric symmetry or employing oblique-angle illumination with retardation effects.[45] While the circular symmetry of isolated TNLNAs' shape leads to an EM response, which is independent of the normal incident light polarization,[33] the out-of-plane vertical stacking of building blocks offers a unique avenue to excite and spectrally tune the dark multipolar modes through the out-of-plane mode hybridization without altering the overall size and footprint.[45]

In conclusion, fixed-size tapered-shape nanolaminate nanoantennas (TNLNAs) composed of vertically stacked MIM plasmonic building blocks can exhibit tunable double-resonant optical responses by out-of-plane engineering of the metal-to-insulator thickness ratio controlled by thin-film deposition. Numerical studies reveal that TNLNAs support two magnetoelectric modes from the hybridization of elementary modes in vertically stacked MIM building blocks. Moreover, being spatially overlapped, the two magnetoelectric modes show large resonant optical cross sections, significant field enhancements, and broad spectral tunability in the visible-to-near-infrared regime. Hence, spectrally tunable double-resonant TNLNAs are suitable for direct integration with other nanodevices of a predefined footprint for multimodal operations, especially in nano-bio interfacing applications requiring constrained structural design and minimized geometric variations.

See the supplementary material for fabrication procedure details, experimental setup, simulation parameters, and supporting near-field calculations.

AUTHORS' CONTRIBUTIONS

E.M. and Y.Q. contributed equally to this work.

DATA AVAILABILITY

The data that support the findings of this study are available from the corresponding author upon reasonable request.

REFERENCES

[1] S.-Y. Ding, J. Yi, J.-F. Li, B. Ren, D.-Y. Wu, R. Panneerselvam, and Z.-Q. Tian, Nat. Rev. Mater. **1**(6), 16021 (2016).

[2] J. N. Anker, W. P. Hall, O. Lyandres, N. C. Shah, J. Zhao, and R. P. Van Duyne, Nat. Mater. **7**(6), 442–453 (2008).

[3] M. Pelton, Nat. Photonics **9**(7), 427–435 (2015).

[4] M. Kauranen and A. V. Zayats, Nat. Photonics **6**(11), 737–748 (2012).

[5] X. Huang, P. K. Jain, I. H. El-Sayed, and M. A. El-Sayed, Lasers Med. Sci. **23**(3), 217–228 (2008).

[6] P. Bazard, R. D. Frisina, J. P. Walton, and V. R. Bhethanabotla, Sci. Rep. **7**(1), 7803 (2017).

[7] L. Bonacina, P.-F. Brevet, M. Finazzi, and M. Celebrano, J. Appl. Phys. **127**(23), 230901 (2020).

[8] M. L. Brongersma, N. J. Halas, and P. Nordlander, Nat. Nanotechnol. **10**(1), 25–34 (2015).

[9] G. Baffou, R. Quidant, and F. J. G. de Abajo, ACS Nano **4**(2), 709–716 (2010).

[10] S. A. Safiabadi Tali and W. Zhou, Nanophotonics **8**(7), 1199–1225 (2019).

[11] E. K. Payne, K. L. Shuford, S. Park, G. C. Schatz, and C. A. Mirkin, J. Phys. Chem. B **110**(5), 2150–2154 (2006).

[12] E.-A. You, W. Zhou, J. Y. Suh, M. D. Huntington, and T. W. Odom, ACS Nano **6**(2), 1786–1794 (2012).

[13] H. Harutyunyan, G. Volpe, R. Quidant, and L. Novotny, Phys. Rev. Lett. **108**(21), 217403 (2012).

[14] K. Thyagarajan, S. Rivier, A. Lovera, and O. J. F. Martin, Opt. Express **20**(12), 12860–12865 (2012).

[15] K. Thyagarajan, J. Butet, and O. J. F. Martin, Nano Lett. **13**(4), 1847–1851 (2013).

[16] Y. Zhang, F. Wen, Y.-R. Zhen, P. Nordlander, and N. J. Halas, Proc. Natl. Acad. Sci. U. S. A. **110**(23), 9215 (2013).

[17] H. Wang, D. W. Brandl, F. Le, P. Nordlander, and N. J. Halas, Nano Lett. **6**(4), 827–832 (2006).

[18] R. Bardhan, S. Mukherjee, N. A. Mirin, S. D. Levit, P. Nordlander, and N. J. Halas, J. Phys. Chem. C **114**(16), 7378–7383 (2010).

[19] S. Mukherjee, H. Sobhani, J. B. Lassiter, R. Bardhan, P. Nordlander, and N. J. Halas, Nano Lett. **10**(7), 2694–2701 (2010).

[20] S. Hong, J. A. I. Acapulco, H. Y. Jang, and S. Park, Chem. Mater. **26**(12), 3618–3623 (2014).

[21] E. Ozbay, Science **311**(5758), 189 (2006).

[22] M. Dipalo, G. C. Messina, H. Amin, R. L. Rocca, V. Shalabaeva, A. Simi, A. Maccione, P. Zilio, L. Berdondini, and F. De Angelis, Nanoscale **7**(8), 3703–3711 (2015).

[23] R. L. Rocca, G. C. Messina, M. Dipalo, V. Shalabaeva, and F. De Angelis, Small **11**(36), 4632–4637 (2015).

[24] A. E. Nel, L. Mädler, D. Velegol, T. Xia, E. M. V. Hoek, P. Somasundaran, F. Klaessig, V. Castranova, and M. Thompson, Nat. Mater. **8**, 543 (2009).

[25] A. Poddubny, I. Iorsh, P. Belov, and Y. Kivshar, Nat. Photonics **7**(12), 948–957 (2013).

[26] J. Song and W. Zhou, Nano Lett. **18**(7), 4409–4416 (2018).

[27] Y. Qian, S. A. Safiabadi Tail, E. Mejia, and W. Zhou, Optik **230**, 166332 (2021).

[28] W. Nam, J. Song, S. A. Safiabadi Tali, H. J. Lezec, A. Agrawal, and W. Zhou, ACS Appl. Nano Mater. **4**(3), 3175–3184 (2021).

[29] A. Dmitriev, T. Pakizeh, M. Käll, and D. S. Sutherland, Small **3**(2), 294–299 (2007).

[30] M. Frederiksen, V. E. Bochenkov, R. Ogaki, and D. S. Sutherland, Nano Lett. **13**(12), 6033–6039 (2013).

[31] M. Kuttge, F. J. García de Abajo, and A. Polman, Nano Lett. **10**(5), 1537–1541 (2010).

[32] N. Maccaferri, Y. Zhao, T. Isoniemi, M. Iarossi, A. Parracino, G. Strangi, and F. De Angelis, Nano Lett. **19**(3), 1851–1859 (2019).

[33] K. L. Domina, V. V. Khardikov, V. Goryashko, and A. Y. Nikitin, Adv. Opt. Mater. **8**(5), 1900942 (2020).

[34] G. Schaffernak, M. K. Krug, M. Belitsch, M. Gašparić, H. Ditlbacher, U. Hohenester, J. R. Krenn, and A. Hohenau, ACS Photonics **5**(12), 4823–4827 (2018).

[35] R. Verre, Z. J. Yang, T. Shegai, and M. Käll, Nano Lett. **15**(3), 1952–1958 (2015).

[36] Y. Ekinci, A. Christ, M. Agio, O. J. F. Martin, H. H. Solak, and J. F. Löffler, Opt. Express **16**(17), 13287–13295 (2008).

[37] J. Henzie, M. H. Lee, and T. W. Odom, Nat. Nanotechnol. **2**(9), 549–554 (2007).

[38] A. Mooradian, Phys. Rev. Lett. **22**(5), 185–187 (1969).

[39] L. Jiang, T. Yin, Z. Dong, M. Liao, S. J. Tan, X. M. Goh, D. Allioux, H. Hu, X. Li, and J. K. Yang, ACS Nano **9**(10), 10039–10046 (2015).

[40] A. Derkachova, K. Kolwas, and I. Demchenko, Plasmonics **11**(3), 941–951 (2016).

[41] R. Alaee, M. Albooyeh, M. Yazdi, N. Komjani, C. Simovski, F. Lederer, and C. Rockstuhl, Phys. Rev. B **91**(11), 115119 (2015).

[42] S. Deng, R. Li, J.-E. Park, J. Guan, P. Choo, J. Hu, P. J. M. Smeets, and T. W. Odom, Proc. Natl. Acad. Sci. U. S. A. **117**(38), 23380–23384 (2020).

[43] W. A. Britton, Y. Chen, and L. Dal Negro, Opt. Mater. Express **9**(2), 878–891 (2019).

[44] M. S. Bin-Alam, O. Reshef, Y. Mamchur, M. Z. Alam, G. Carlow, J. Upham, B. T. Sullivan, J.-M. Ménard, M. J. Huttunen, R. W. Boyd, and K. Dolgaleva, Nat. Commun. **12**(1), 974 (2021).

[45] D. E. Gómez, Z. Q. Teo, M. Altissimo, T. J. Davis, S. Earl, and A. Roberts, Nano Lett. **13**(8), 3722–3728 (2013).